MIT Libraries | DSpace@MIT

MIT Open Access Articles

Unsteady Adjoint of Pressure Loss for a Fundamental Transonic Turbine Vane

The MIT Faculty has made this article openly available. ***Please share*** how this access benefits you. Your story matters.

Citation: Talnikar, Chaitanya et al. "Unsteady Adjoint of Pressure Loss for a Fundamental Transonic Turbine Vane." Journal of Turbomachinery 139, 3 (November 2016): 031001 © 2017 ASME

As Published: http://dx.doi.org/10.1115/1.4034800

Publisher: ASME International

Persistent URL: http://hdl.handle.net/1721.1/114775

Version: Final published version: final published article, as it appeared in a journal, conference proceedings, or other formally published context

Terms of Use: Article is made available in accordance with the publisher's policy and may be subject to US copyright law. Please refer to the publisher's site for terms of use.

Massachusetts Institute of Technology

Unsteady Adjoint of Pressure Loss for a Fundamental Transonic Turbine Vane

Chaitanya Talnikar[1]
Aerospace Computational Design Laboratory,
Department of Aerospace and Astronautics,
Massachusetts Institute of Technology,
Cambridge, MA 02139
e-mail: talnikar@mit.edu

Qiqi Wang
Aerospace Computational Design Laboratory,
Department of Aerospace and Astronautics,
Massachusetts Institute of Technology,
Cambridge, MA 02139
e-mail: qiqi@mit.edu

Gregory M. Laskowski
Engineering Technologies,
GE Aviation,
Lynn, MA 01910
e-mail: laskowski@ge.com

High-fidelity simulations, e.g., large eddy simulation (LES), are often needed for accurately predicting pressure losses due to wake mixing and boundary layer development in turbomachinery applications. An unsteady adjoint of high-fidelity simulations is useful for design optimization in such aerodynamic applications. In this paper, we present unsteady adjoint solutions using a large eddy simulation model for an inlet guide vane from von Karman Institute (VKI) using aerothermal objectives. The unsteady adjoint method is effective in capturing the gradient for a short time interval aerothermal objective, whereas the method provides diverging gradients for long time-averaged thermal objectives. As the boundary layer on the suction side near the trailing edge of the vane is turbulent, it poses a challenge for the adjoint solver. The chaotic dynamics cause the adjoint solution to diverge exponentially from the trailing edge region when solved backward in time. This results in the corruption of the sensitivities obtained from the adjoint solutions. An energy analysis of the unsteady compressible Navier–Stokes adjoint equations indicates that adding artificial viscosity to the adjoint equations can dissipate the adjoint energy while potentially maintaining the accuracy of the adjoint sensitivities. Analyzing the growth term of the adjoint energy provides a metric for identifying the regions in the flow where the adjoint term is diverging. Results for the vane obtained from simulations performed on the Titan supercomputer are demonstrated. [DOI: 10.1115/1.4034800]

Introduction

High-fidelity simulations, like large eddy simulations (LESs), are essential for accurately simulating turbulent fluid flows. This is especially true for turbomachinery applications, which exhibit complex flow phenomena like a transitioning boundary layer and flow separation. Gourdain et al. [1] compared LES to low fidelity methods like Reynolds-averaged Navier–Stokes (RANS) simulations and found that LES predicts heat transfer with a much higher accuracy, matching with experimental data. Moreover, LES is becoming feasible with the rapid growth in the power of supercomputers. In just over a decade, compute capacity has increased by a factor of 100. This has enabled high-fidelity simulations for fluid problems where the Reynolds number is on the order of a million.

For accomplishing design of turbomachinery components using LES in a reasonable amount of time, it is necessary to obtain gradients of design objectives with respect to design parameters. A straightforward method to obtain gradients is to use finite difference, but the number of simulations required scales linearly with the number of input parameters. An alternative is to use the adjoint method, which provides the gradient with respect to a large number of parameters using just one additional simulation. This method has been used extensively for performing design optimization using steady-state Euler [2] and RANS [3] simulations. The adjoint method involves solving a set of equations known as the adjoint equations. For a time-dependent simulation like LES, an unsteady adjoint method is required, in which the adjoint equations are simulated backward in time to obtain the desired derivatives. Recently, Economon et al. [4] performed unsteady adjoint simulations for a rotating airfoil, but these were restricted to unsteady laminar fluid flows.

It has been observed in numerous studies [5,6] and through simulations conducted for this paper, that for turbulent fluid flows, the unsteady adjoint solution grows exponentially when simulated backward in time. This is due to the chaotic nature of the turbulent flow field. From chaos theory [7], it is known that the solution of certain nonlinear partial differential equations is sensitive to perturbations to initial conditions or parameters. The solutions of the Navier–Stokes equations are believed to exhibit this property and the behavior has been demonstrated numerically and experimentally [8]. The divergence to infinity of the adjoint field makes it unusable for computing sensitivities of the objective with respect to perturbations in input parameters.

This paper presents a possible solution to this problem by controlling the growth of the adjoint field. An energy analysis of the unsteady compressible Navier–Stokes adjoint equations reflects that a single term contributes to the growth of the energy of the adjoint field, while another viscouslike term dissipates the adjoint energy. This suggests the idea that adding artificial viscosity to the adjoint equations can dampen the adjoint fields. The maximum singular value of the growth term matrix gives an indication of the regions in the flow where the adjoint term is diverging at an exponential rate. By the addition of minimal artificial viscosity in these regions, the growth of the adjoint energy can be curbed, and at the same time, the accuracy of the derivatives obtained from the adjoint solutions can potentially be maintained.

Problem Setup

The turbomachinery problem of interest is transonic flow over a highly loaded turbine inlet guide vane, designed by researchers at von Karman Institute (VKI) [9], shown in Fig. 1.

[1]Corresponding author.

Contributed by the International Gas Turbine Institute (IGTI) of ASME for publication in the JOURNAL OF TURBOMACHINERY. Manuscript received August 29, 2016; final manuscript received September 9, 2016; published online November 8, 2016. Editor: Kenneth Hall.

 Copyright © 2017 by ASME

Downloaded From: http://turbomachinery.asmedigitalcollection.asme.org/ on 04/12/2018 Terms of Use: http://www.asme.org/about-asme/terms-of-use

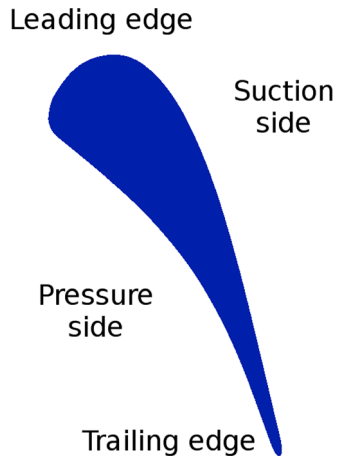

Fig. 1 Turbine vane geometry

Subsonic flow enters from the inlet upstream of the vane, accelerates as it goes around the suction side, and reaches close to the speed of sound near the trailing edge of the vane. The boundary layer transitions from laminar to turbulent at the suction side, near the trailing edge, as shown in Fig. 2. The point of transition is highly dependent on the turbulent intensity of the flow at the inlet. The flow then separates at the trailing edge, producing a turbulent wake. Due to boundary layer development on the suction and pressure sides and mixing in the wake, there is a significant loss in stagnation pressure of the fluid.

The Reynolds number for this setup is 10^6. The isentropic Mach number is 0.9. The vane has a chord length of 67.647 mm and is at an angle of $\gamma = 55$ deg to the axial direction, which is the same as the inlet flow direction. The vanes are in a linear cascade and the pitch is 0.85 times the chord length. In the simulation, periodic boundary conditions are imposed on the top and bottom. The spanwise extent of the numerical setup is restricted to 10 mm. Numerical studies have shown that this is sufficient to capture the dynamics of turbulence for this problem [1]. The vane surface is assumed to be isothermal.

The design objective for this problem is an infinite time-averaged and mass flow-averaged stagnation pressure loss coefficient ($\bar{p}_l$), 16 mm downstream of the vane on a surface parallel to the inlet plane. As mentioned before, due to boundary layer development and mixing in the wake downstream of the vane, there is a large drop in the stagnation pressure, which leads to loss in performance, as shown in Fig. 3. Hence, there is an interest in minimizing the pressure loss. In practice, the time average for the objective is performed for an interval, which is sufficient to

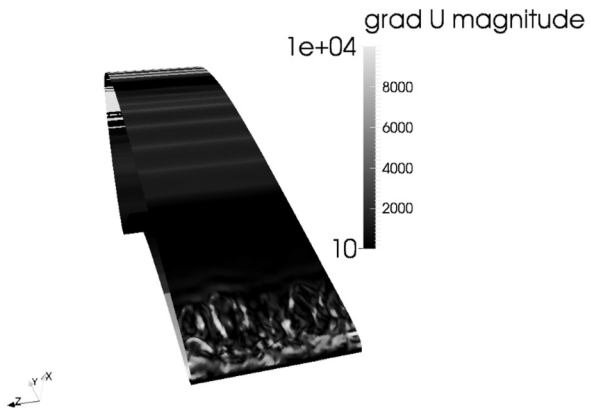

Fig. 2 Contour plot of shear stress on the surface of the vane. Nondimensionalized with respect to flow velocity Mach 0.9. Reynolds number 1×10^6, turbulent intensity 1%.

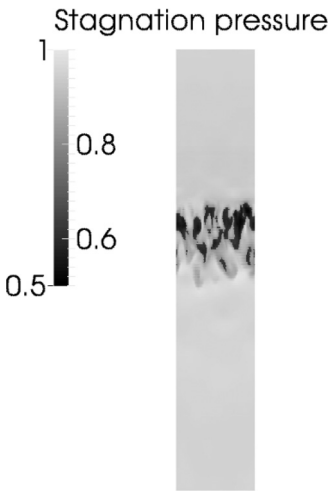

Fig. 3 Stagnation pressure on a vertical spanwise cross section 10 mm downstream of the trailing edge of the vane. Nondimensionalized with respect to inlet stagnation pressure.

provide a reasonably accurate estimate of the infinite time average. In this problem, it is equal to the time it takes for the flow to pass from the inlet to the outlet, which comes to be approximately 2 ms. Though the interval length might seem small, it encompasses several time scales of the turbulence in the wake. The formula for $\bar{p}_l$ is

$$\bar{p}_l = \frac{\bar{p}_{t,l}}{p_{t,\text{in}}} \tag{1}$$

$$\bar{p}_{t,l} = \lim_{T\to\infty} \frac{1}{T} \int_0^T \frac{\int_S \rho_p u_n (p_{t,\text{in}} - p_{t,p}) dS}{\int_S \rho_p u_n dS} dt \tag{2}$$

$$p_{t,p} = p_p \left(1 + \frac{\gamma - 1}{2} M_p^2\right)^{\frac{\gamma}{\gamma-1}} \tag{3}$$

Time-Averaged Objectives. Observations of turbulent flows indicate that statistics of turbulence like time-averaged mean of pressure loss coefficient are well-defined, stable quantities [10,11]. Other than relatively rare cases that exhibit flow hysteresis, these statistics are insensitive to initial conditions. In dynamical systems theory, an autonomous system is called ergodic if infinite time averages are independent of initial condition. An infinite time average of such ergodic systems is proven to be differentiable to parameters of the system, under additional assumptions [12,13]. This theory is consistent with observations in turbulent flows, in which the statistics are found to depend continuously on parameters when the flow is away from bifurcations [14]. Hence, we assume that the pressure loss coefficient is smooth as a function of inputs, like source term perturbations to the compressible Navier–Stokes equations and shape parameters, or in other words at least the first derivative exists. In this particular problem, the averaging is started after simulating the system to a statistically stationary state, which took about five flow throughs starting from a uniform zero velocity initial condition. Figure 4 shows the convergence of the pressure loss coefficient objective as the averaging interval is increased.

Physics. The problem can be physically modeled using the compressible Navier–Stokes equations, with the ideal gas law as

Downloaded From: http://turbomachinery.asmedigitalcollection.asme.org/ on 04/12/2018 Terms of Use: http://www.asme.org/about-asme/terms-of-use

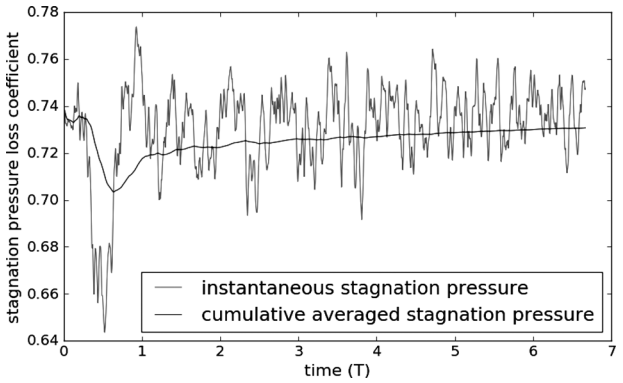

Fig. 4 Instantaneous and time-averaged stagnation pressure loss coefficient for the vane. *X*-axis denotes the time normalized by the time it takes for the flow to pass from the inlet to outlet.

an approximation for the state equation, and appropriate inlet, outlet, and wall boundary conditions

$$\begin{aligned}
&\text{In } \mathbf{x} \in D, t \in [0,T] \\
&\frac{\partial \rho}{\partial t} + \nabla \cdot (\rho \mathbf{u}) = 0 \\
&\frac{\partial (\rho \mathbf{u})}{\partial t} + \nabla \cdot (\rho \mathbf{u}\mathbf{u}) + \nabla p = \nabla \cdot \sigma \\
&\frac{\partial (\rho E)}{\partial t} + \nabla \cdot (\rho E \mathbf{u} + p\mathbf{u}) = \nabla \cdot (\mathbf{u} \cdot \sigma + \alpha \nabla e) \\
&\sigma = \mu(\nabla \mathbf{u} + \nabla \mathbf{u}^{\mathrm{T}}) - \frac{2\mu}{3}(\nabla \cdot \mathbf{u})\mathbf{I} \\
&p = (\gamma - 1)\rho e \\
&e = E - \frac{\mathbf{u} \cdot \mathbf{u}}{2}
\end{aligned} \tag{4}$$

For simulating turbulence, LES provides a way for resolving the large-scale features of the flow and modeling the small-scale structures. Traditionally, when performing an LES, a subgrid scale (SGS) model like Smagorinsky or Vreman [15] is used, but as this problem is simulated using a second-order finite volume method, no SGS model is used. This approach in literature is known as implicit LES (ILES). It has been shown that when using a lower order method, the numerical viscosity from the grid might be of the same order as the subgrid scale viscosity [16].

Numerical Methods. The flow solver is written in Python, with the help of numpy, scipy, cython, and petsc4py libraries. It discretizes the Navier–Stokes equations over general unstructured meshes using the second-order finite volume method. A total variation diminishing face reconstruction scheme is used for shock capturing. For time marching, a strong stability preserving third-order Runge–Kutta (RK) method [17] is used. An approximate Roe [18] solver is employed for propagating shocks and discontinuities. Nonreflecting boundary conditions are used for the inlet and outlet. Parallelization is accomplished using the message passing interface (MPI) library for Python, mpi4py.

The computational domain of the problem is shown in Fig. 5. The simulations are performed on a 2D and 3D version of the problem. The 3D mesh is just the 2D mesh extended to 3D and discretized uniformly in the spanwise direction. The mesh is a hybrid structured/unstructured mesh. It is structured in the inlet, outlet regions and around the surface of the vane, and is unstructured in the remaining areas. The smallest cell size is maintained below 0.5 mm in regions away from the wall. This corresponds to a ratio of 4 between the Kolmogorov length scale and cell size at the inlet of the flow. To capture all the significant eddies of the flow near the wall (such an LES is called a wall-resolved LES), the wall normal cell width has to be below 1 in terms of wall units [19]. This puts a constraint on the time step to be of the order of a few nanoseconds, tremendously increasing the simulation cost. To be able to run the simulation in a reasonable time frame, the maximum $y+$ is kept at 10, $z+$ at 25, and $x+$ at 150. This results in an under-resolved LES. In the future, a wall model might help alleviate this problem by allowing the mesh to have a higher $y+$. For now, the simulations are run without any wall model to get preliminary unsteady adjoint results.

Unsteady Adjoint

The unsteady adjoint method provides a way for computing derivatives of an objective dependent on the state of a system, with respect to input parameters, where the state is constrained by a time-dependent partial differential equation. Rewriting Eq. (4) in vector form

$$\begin{aligned}
&\frac{\partial \mathbf{w}}{\partial t} + \nabla \cdot \mathbf{F} = \nabla \cdot \mathbf{F}^{\mathbf{v}} \\
&\mathbf{w} = \begin{pmatrix} \rho \\ \rho \mathbf{u} \\ \rho E \end{pmatrix} \\
&\mathbf{F} = \begin{pmatrix} \rho \mathbf{u} \\ \rho \mathbf{u}\mathbf{u} \\ (\rho E + p)\mathbf{u} \end{pmatrix} \\
&\mathbf{F}^{\mathbf{v}} = \begin{pmatrix} 0 \\ \sigma \\ \mathbf{u} \cdot \sigma + \alpha \nabla e \end{pmatrix}
\end{aligned} \tag{5}$$

Using the Einstein summation notation in the Euclidean space, Eq. (5) can be simplified to, with the addition of a source term

$$\frac{\partial w_i}{\partial t} + \frac{\partial F_{ij}}{\partial x_j} = \frac{\partial F^v_{ij}}{\partial x_j} + s_i, i = 1 \ldots 5 \tag{6}$$

Consider a time-averaged objective ($\bar{J}$) on the boundary surface (S). T is a large enough time to estimate the infinite time average with required accuracy. J includes the factor $1/T$

$$\bar{J} = \int_0^T \int_S J(w_i) dS dt \tag{7}$$

The first step in deriving the adjoint equations is to linearize the governing equation and form the Lagrangian

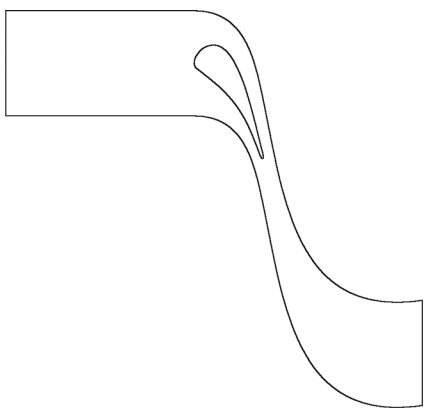

Fig. 5 Turbine vane computational domain

Downloaded From: http://turbomachinery.asmedigitalcollection.asme.org/ on 04/12/2018 Terms of Use: http://www.asme.org/about-asme/terms-of-use

$$\delta\bar{J} = \int_0^T \int_S \left(\frac{\partial J}{\partial w_i}\delta w_i\right) dSdt + \int_0^T \int_V \hat{w}_i \left(\frac{\partial \delta w_i}{\partial t} + \frac{\partial \delta F_{ij} - \delta F^v_{ij}}{\partial x_j} - \delta s_i\right) dVdt \tag{8}$$

Integrating the second term by parts in time and space

$$\begin{aligned}\delta\bar{J} = &\int_0^T \int_S \left(\frac{\partial J}{\partial w_i}\delta w_i\right) dSdt + \int_V \left(\hat{w}_{i|T}\delta w_{i|T} - \hat{w}_{i|0}\delta w_{i|0}\right) dV \\ &- \int_0^T \int_V \frac{\partial \hat{w}_i}{\partial t}\delta w_i dVdt + \int_0^T \int_S \hat{w}_i \left(\delta F_{ij} - \delta F^v_{ij}\right) n_j dSdt \\ &- \int_0^T \int_V \frac{\partial \hat{w}_i}{\partial x_j}\left(\delta F_{ij} - \delta F^v_{ij}\right) dVdt \\ &- \int_0^T \int_V \hat{w}_i \delta s_i dVdt\end{aligned} \tag{9}$$

Differentiating F_{ij} and F^v_{ij} with respect to w_k, F^v_{ij} with respect to $\partial w_k/\partial x_l$

$$A_{ijk} = \frac{\partial F_{ij}}{\partial w_k}, \quad A^v_{ijk} = \frac{\partial F^v_{ij}}{\partial w_k}, \quad D_{ijkl} = \frac{\partial F^v_{ij}}{\partial \dfrac{\partial w_k}{\partial x_l}} \tag{10}$$

The terms can be rearranged to form

$$\begin{aligned}\delta\bar{J} = &\int_0^T \int_S \left[\left(\frac{\partial J}{\partial w_i} + \hat{w}_k \left(A_{kji} - A^v_{kji}\right) n_j\right)\delta w_i - \hat{w}_i D_{ijkl}\delta\frac{\partial w_k}{\partial x_l} n_j\right] dSdt \\ &+ \int_V \left(\hat{w}_{i|T}\delta w_{i|T} - \hat{w}_{i|0}\delta w_{i|0}\right) dV \\ &- \int_0^T \int_V \left(\frac{\partial \hat{w}_i}{\partial t} + \frac{\partial \hat{w}_k}{\partial x_j}\left(A_{kji} - A^v_{kji}\right)\right)\delta w_i dVdt \\ &+ \int_0^T \int_V \frac{\partial \hat{w}_i}{\partial x_j} D_{ijkl}\frac{\partial \delta w_k}{\partial x_l} dVdt \\ &- \int_0^T \int_V \hat{w}_i \delta s_i dVdt\end{aligned} \tag{11}$$

The last term in Eq. (11) can again be integrated by parts to form

$$\begin{aligned}\int_0^T \int_V \frac{\partial \hat{w}_i}{\partial x_j} D_{ijkl}\frac{\partial \delta w_k}{\partial x_l} dVdt = &\int_0^T \int_S \frac{\partial \hat{w}_i}{\partial x_j} D_{ijkl}\delta w_k n_l dSdt \\ &- \int_0^T \int_V \frac{\partial}{\partial x_l}\left(\frac{\partial \hat{w}_i}{\partial x_j} D_{ijkl}\right)\delta w_k dVdt\end{aligned} \tag{12}$$

Using no perturbation in the initial condition, $\delta w_{i|0} = 0$, the adjoint equation comes out to be

$$-\frac{\partial \hat{w}_i}{\partial t} - \left(A_{kji} - A^v_{kji}\right)\frac{\partial \hat{w}_k}{\partial x_j} = \frac{\partial}{\partial x_l}\left(D_{kjil}\frac{\partial \hat{w}_k}{\partial x_j}\right) \tag{13}$$

with boundary condition on the surface

$$\left(\frac{\partial J}{\partial w_i} + \hat{w}_k \left(A_{kji} - A^v_{kji}\right) n_j + \frac{\partial \hat{w}_k}{\partial x_j} D_{kjil} n_l\right)\delta w_i - \hat{w}_i D_{ijkl}\delta\frac{\partial w_k}{\partial x_l} n_j = 0 \tag{14}$$

And terminal condition $\hat{w}_{i,T} = 0$. Notice that there is a terminal condition, which implies that the adjoint equations have to be integrated backward in time. The procedure to compute sensitivity of an objective for a set of perturbations involves solving the compressible Navier–Stokes (primal) equations from time $t = 0$ to T. After this, the adjoint equation is solved backward in time from $t = T$ to 0. The adjoint equation requires the solution of the primal equation at every time t. The sensitivity due to a perturbation in the source term can be obtained using

$$\delta\bar{J} = -\int_0^T \int_V \hat{w}_i \delta s_i dVdt \tag{15}$$

Implementation. In practice, the adjoint equation is implemented as a discrete unsteady adjoint, instead of the continuous unsteady adjoint derived in this section. The discrete adjoint has the advantage that it provides a derivative or adjoint sensitivities that are precise to machine precision when compared with finite difference sensitivities. The discrete adjoint is derived with the help of automatic differentiation, provided by the Python package Theano [20,21]. Additionally, the checkpointing method is used to provide the adjoint equation with the necessary primal solutions at each point in time. This method overcomes the need for storing all the primal solutions (at every time step) in memory by saving snapshots of the primal solution in periodic intervals on disk. When the adjoint is simulated, the primal solutions in an interval are obtained by repeating the primal simulation for that specific interval.

Results. The unsteady adjoint method is tested on the turbine vane problem using an aerothermal objective. A total of 4 simulations are performed, a short time interval and a long time interval simulation on each of the 2D and 3D turbine vane problems. Figure 6 shows a contour plot of the density adjoint field for a cross section of the 3D turbine vane. The adjoint magnitude is large in the trailing edge region and the leading edge. The flow is sensitive to perturbations in this area, leading to the high values of the adjoint flow fields.

The 2D and 3D long time interval unsteady adjoints for the turbine vane diverge exponentially when simulated backward in time, as shown in Fig. 7 for the 3D adjoint. The long time interval 3D unsteady adjoint shows exponential growth throughout the length of the simulation, and its L_2 norm reaches very high magnitudes of around 10^{60}. While conducting these simulations, it was observed that the 2D adjoint diverges at a faster rate than the 3D adjoint. This is because the third dimension provides a way to dissipate the growth in the adjoint flow field.

The high values of the adjoint fields make the adjoint sensitivities worthless in the case of the long time interval 2D unsteady adjoint ($T = 0.1$) and 3D unsteady adjoint ($T = 1$) simulations, where T is the simulation time normalized with respect to a single flow through time. Table 1 gives the actual values of the sensitivities of the aerothermal objective with respect to Gaussian shaped source term perturbations, in the conservative flow fields upstream

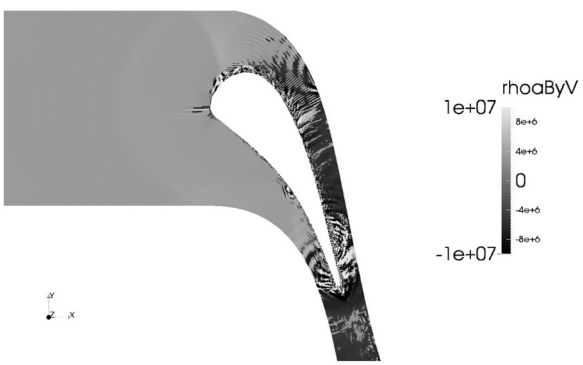

Fig. 6 A visualization of the density adjoint field from halfway through a short time 3D unsteady adjoint simulation

Downloaded From: http://turbomachinery.asmedigitalcollection.asme.org/ on 04/12/2018 Terms of Use: http://www.asme.org/about-asme/terms-of-use

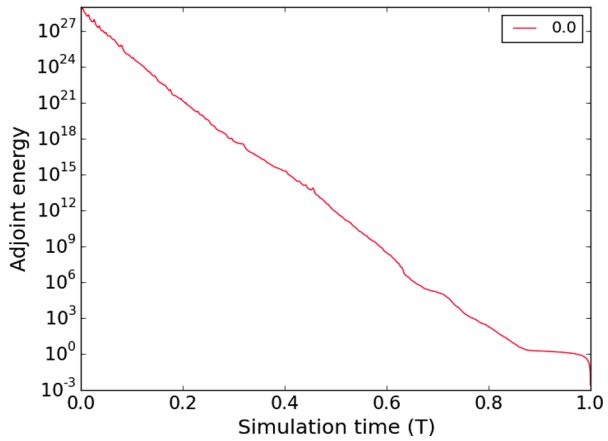

Fig. 7 Growth of energy norm of adjoint fields for different simulations. *Y*-axis shows energy norm of a dimensional conservative adjoint field.

Table 1 Comparison between adjoint and finite difference sensitivities for a heat transfer objective

Simulation	T	Finite diff.	Adjoint
2D	0.01	4.340×10^{-5}	4.341×10^{-5}
2D	0.1	0.00695	640041
3D	0.1	0.005904	0.005923
3D	1	0.00710	$\sim 10^{34}$

of the vane. The short time interval 2D and 3D unsteady adjoint simulations provide the correct sensitivities. This is because the L_2 norm of the adjoint fields is relatively small for most of the simulation time. This result shows that for an objective which only requires a short time average, the unsteady adjoint method can provide the correct gradient.

Stabilizing Adjoint Equations

Due to the chaotic nature of a turbulent fluid flow, the L_2 norm of an unsteady adjoint solution diverges exponentially when the adjoint equations are solved backward in time. This is primarily due to the sensitivity of the solution field with respect to small perturbations in the initial flow field or parameters of the fluid system

$$\|\hat{w}\|_{L_2(D)} = \left(\int_V \hat{w}_i \hat{w}_i dV \right)^{\frac{1}{2}} \tag{16}$$

Wang and Gao [5] performed an energy norm analysis of the adjoint equations for a fluid flow governed by the incompressible Navier–Stokes equations, and found out that there are two terms which govern the change in adjoint energy of the system. The first is a growth term, which is large in regions where the matrix norm of $\nabla \mathbf{u}$ is large, meaning that regions having large gradients in velocity contribute to the divergence of adjoint energy. The second is a dissipation term, which tries to reduce the adjoint energy and is scaled by the viscosity of the fluid. The adjoint energy diverges to infinity when the growth term dominates the dissipation term. This analysis shows that if additional viscosity is added to the adjoint equations, the dissipation term can limit the growth of the adjoint field.

Blonigan et al. [6] performed numerical experiments of adding uniform artificial viscosity to the adjoint equations and was successful in inhibiting the exponential growth of the adjoint field. But, this also resulted in the corruption of the sensitivities obtained from the adjoint solution. A potential fix to the latter problem is to add viscosity to the adjoint equations only in certain regions of the fluid flow where the adjoint field has a high rate of growth. This idea is explored by applying the energy analysis method on the unsteady adjoint of the compressible Navier–Stokes equations.

Symmetrization. Performing the energy analysis on the adjoint of the conservative Navier–Stokes equations is cumbersome. It is more useful to perform it on the adjoint of the symmetrized Navier Stokes equations. It can be shown that if the adjoint energy norm of the symmetrized equations is bounded, then the adjoint energy of the conservative equations is also bounded. Hence, from here on, the focus will be on the adjoint of the symmetrized equations.

Symmetrization of the Navier–Stokes equations means making the tensors A_{ijk} and D_{ijkl} symmetric in i and k. The analysis is performed on the Euler equations, but the symmetrization procedure also works out for the compressible Navier–Stokes equations, as demonstrated in Ref. [22]. Using the quasi-linear form of the Euler equation

$$\frac{\partial w_i}{\partial t} + A_{ijk} \frac{\partial w_k}{\partial x_j} = 0 \tag{17}$$

Symmetrizing by a transformation of the conservative variables to symmetrized variables, $\delta v_i = T_{ik} \delta w_k$

$$T_{ik}^{-1} \frac{\partial v_k}{\partial t} + A_{ijk} T_{km}^{-1} \frac{\partial v_m}{\partial x_j} = 0 \tag{18}$$

Premultiplying by T_{li}

$$\frac{\partial v_l}{\partial t} + T_{li} A_{ijk} T_{km}^{-1} \frac{\partial v_m}{\partial x_j} = 0 \tag{19}$$

T can be chosen such that $\hat{A}_{ljm} = T_{li} A_{ijk} T_{km}^{-1}$ is symmetric, giving the symmetrized Euler equations

$$\frac{\partial v_l}{\partial t} + \hat{A}_{ljm} \frac{\partial v_m}{\partial x_j} = 0 \tag{20}$$

The symmetrizer from primitive to symmetric variables, $\delta v_i = S_{ik} \delta q_i$ is

$$S = \begin{pmatrix} \frac{c}{\sqrt{\gamma}\rho} & 0 & 0 & 0 & 0 \\ 0 & 1 & 0 & 0 & 0 \\ 0 & 0 & 1 & 0 & 0 \\ 0 & 0 & 0 & 1 & 0 \\ -\frac{c}{\rho\sqrt{\gamma(\gamma-1)}} & 0 & 0 & 0 & \sqrt{\frac{\gamma}{\gamma-1}} \frac{1}{\rho c} \end{pmatrix} \tag{21}$$

The transformation from conservative to primitive variables is $\delta q_i = V_{ik} \delta w_i$

$$V = \begin{pmatrix} 1 & 0 & 0 & 0 & 0 \\ \frac{u_1}{\rho} & \frac{1}{\rho} & 0 & 0 & 0 \\ \frac{u_2}{\rho} & 0 & \frac{1}{\rho} & 0 & 0 \\ \frac{u_3}{\rho} & 0 & 0 & \frac{1}{\rho} & 0 \\ \frac{(\gamma-1)u_i u_i}{2} & -(\gamma-1)u_1 & -(\gamma-1)u_2 & -(\gamma-1)u_3 & (\gamma-1) \end{pmatrix} \tag{22}$$

with $T_{ik} = S_{ij} V_{jk}$.

Downloaded From: http://turbomachinery.asmedigitalcollection.asme.org/ on 04/12/2018 Terms of Use: http://www.asme.org/about-asme/terms-of-use

$\hat{A}_{ijk}$ is given by

$$\hat{\boldsymbol{A}}_{:1:} = \begin{pmatrix} u_1 & \frac{c}{\sqrt{\gamma}} & 0 & 0 & 0 \\ \frac{c}{\sqrt{\gamma}} & u_1 & 0 & 0 & \sqrt{\frac{\gamma-1}{\gamma}}c \\ 0 & 0 & u_1 & 0 & 0 \\ 0 & 0 & 0 & u_1 & 0 \\ 0 & \sqrt{\frac{\gamma-1}{\gamma}}c & 0 & 0 & u_1 \end{pmatrix} \tag{23}$$

$$\hat{\boldsymbol{A}}_{:2:} = \begin{pmatrix} u_2 & 0 & \frac{c}{\sqrt{\gamma}} & 0 & 0 \\ 0 & u_2 & 0 & 0 & 0 \\ \frac{c}{\sqrt{\gamma}} & 0 & u_2 & 0 & \sqrt{\frac{\gamma-1}{\gamma}}c \\ 0 & 0 & 0 & u_2 & 0 \\ 0 & 0 & \sqrt{\frac{\gamma-1}{\gamma}}c & 0 & u_2 \end{pmatrix} \tag{24}$$

$$\hat{\boldsymbol{A}}_{:3:} = \begin{pmatrix} u_3 & 0 & 0 & \frac{c}{\sqrt{\gamma}} & 0 \\ 0 & u_3 & 0 & 0 & 0 \\ 0 & 0 & u_3 & 0 & 0 \\ \frac{c}{\sqrt{\gamma}} & 0 & 0 & u_3 & \sqrt{\frac{\gamma-1}{\gamma}}c \\ 0 & 0 & 0 & \sqrt{\frac{\gamma-1}{\gamma}}c & u_3 \end{pmatrix} \tag{25}$$

The adjoint equation for the symmetrized equation comes out to be slightly different, as $\hat{A}_{ljm}$ is not a Jacobian of the flux term of the symmetric variables

$$\delta\bar{J} = \int_0^T \int_S \left(\frac{\partial J}{\partial v_i}\delta v_i\right) dSdt + \int_0^T \int_V \hat{v}_i \left(\frac{\partial \delta v_i}{\partial t} + \hat{A}_{ijk}\frac{\partial \delta v_k}{\partial x_j} + \delta\hat{A}_{ijk}\frac{\partial v_k}{\partial x_j}\right) dVdt \tag{26}$$

Linearizing $\hat{A}_{ijk}$ using $B_{ijkl} = \partial\hat{A}_{ijk}/\partial v_l$ and integrating by parts in time and space

$$\begin{aligned}\delta\bar{J} = &\int_0^T \int_S \left(\frac{\partial J}{\partial v_i}\delta v_i\right) dSdt \\ &+ \int_V \left(\hat{v}_{i|T}\delta v_{i|T} - \hat{v}_{i|0}\delta v_{i|0}\right) dV - \int_0^T \int_V \frac{\partial \hat{v}_i}{\partial t}\delta v_i dVdt \\ &+ \int_0^T \int_S \hat{v}_i \hat{A}_{ijk}\delta v_k n_j dS - \int_0^T \int_V \frac{\partial\left(\hat{v}_i\hat{A}_{ijk}\right)}{\partial x_j}\delta v_k dVdt \\ &+ \int_0^T \int_V \hat{v}_i B_{ijkl}\delta v_l \frac{\partial v_k}{\partial x_j} dVdt\end{aligned} \tag{27}$$

giving rise to the adjoint equation

$$-\frac{\partial \hat{v}_i}{\partial t} - \hat{A}_{kji}\frac{\partial \hat{v}_k}{\partial x_j} - \left(B_{kjil} - B_{kjli}\right)\frac{\partial v_l}{\partial x_j}\hat{v}_k = 0 \tag{28}$$

The viscous term follows the same derivation process as done for the conservative adjoint with one important difference, the $\mathbf{F}^{\mathbf{v}}$ term is considered to be purely a function of $\nabla\,\mathbf{v}$ on the assumption that μ/ρ and α/ρ are constant for linearization purposes. This is also known as the frozen viscosity assumption and implies that the A^v_{kji} term can be ignored. The $\hat{D}_{ijkl}$ tensor comes out to be

$$\hat{\boldsymbol{D}}_{:1:1} = \begin{pmatrix} 0 & 0 & 0 & 0 & 0 \\ 0 & \frac{4}{3}\frac{\mu}{\rho} & 0 & 0 & 0 \\ 0 & 0 & \frac{\mu}{\rho} & 0 & 0 \\ 0 & 0 & 0 & \frac{\mu}{\rho} & 0 \\ 0 & 0 & 0 & 0 & \frac{\gamma\alpha}{\rho} \end{pmatrix} \tag{29}$$

$$\hat{\boldsymbol{D}}_{:2:2} = \begin{pmatrix} 0 & 0 & 0 & 0 & 0 \\ 0 & \frac{\mu}{\rho} & 0 & 0 & 0 \\ 0 & 0 & \frac{4}{3}\frac{\mu}{\rho} & 0 & 0 \\ 0 & 0 & 0 & \frac{\mu}{\rho} & 0 \\ 0 & 0 & 0 & 0 & \frac{\gamma\alpha}{\rho} \end{pmatrix} \tag{30}$$

$$\hat{\boldsymbol{D}}_{:3:3} = \begin{pmatrix} 0 & 0 & 0 & 0 & 0 \\ 0 & \frac{\mu}{\rho} & 0 & 0 & 0 \\ 0 & 0 & \frac{\mu}{\rho} & 0 & 0 \\ 0 & 0 & 0 & \frac{4}{3}\frac{\mu}{\rho} & 0 \\ 0 & 0 & 0 & 0 & \frac{\gamma\alpha}{\rho} \end{pmatrix} \tag{31}$$

$$\hat{\boldsymbol{D}}_{:1:2} = \hat{\boldsymbol{D}}_{:2:1} = \frac{1}{2}\begin{pmatrix} 0 & 0 & 0 & 0 & 0 \\ 0 & 0 & \frac{1}{3}\frac{\mu}{\rho} & 0 & 0 \\ 0 & \frac{1}{3}\frac{\mu}{\rho} & 0 & 0 & 0 \\ 0 & 0 & 0 & 0 & 0 \\ 0 & 0 & 0 & 0 & 0 \end{pmatrix} \tag{32}$$

$$\hat{\boldsymbol{D}}_{:1:3} = \hat{\boldsymbol{D}}_{:3:1} = \frac{1}{2}\begin{pmatrix} 0 & 0 & 0 & 0 & 0 \\ 0 & 0 & 0 & \frac{1}{3}\frac{\mu}{\rho} & 0 \\ 0 & 0 & 0 & 0 & 0 \\ 0 & \frac{1}{3}\frac{\mu}{\rho} & 0 & 0 & 0 \\ 0 & 0 & 0 & 0 & 0 \end{pmatrix} \tag{33}$$

$$\hat{\boldsymbol{D}}_{:2:3} = \hat{\boldsymbol{D}}_{:3:2} = \frac{1}{2}\begin{pmatrix} 0 & 0 & 0 & 0 & 0 \\ 0 & 0 & 0 & 0 & 0 \\ 0 & 0 & 0 & \frac{1}{3}\frac{\mu}{\rho} & 0 \\ 0 & 0 & \frac{1}{3}\frac{\mu}{\rho} & 0 & 0 \\ 0 & 0 & 0 & 0 & 0 \end{pmatrix} \tag{34}$$

As mentioned before, if the conservative adjoint field at any point of time is bounded, then the symmetrized adjoint field is bounded and the vice versa is also true. This can be shown in the following way; the sensitivity due to a perturbation can be computed from either the conservative adjoint solution or symmetrized adjoint solution

$$\begin{aligned}\delta\bar{J} &= -\int_0^T \int_V \hat{w}_i \delta s_i dVdt \\ &= -\int_0^T \int_V \hat{v}_k \delta s_k^v dVdt = -\int_0^T \int_V \hat{v}_k T_{ki}\delta s_i dVdt\end{aligned} \tag{35}$$

So

$$\hat{w}_i = T_{ki}\hat{v}_i \tag{36}$$

Downloaded From: http://turbomachinery.asmedigitalcollection.asme.org/ on 04/12/2018 Terms of Use: http://www.asme.org/about-asme/terms-of-use

$$\|\hat{\mathbf{w}}\|_{L_2(D)} \leq \|\mathbf{T}^{\mathrm{T}}\|_{L_2(D)}\|\hat{\mathbf{v}}\|_{L_2(D)} \tag{37}$$

The transformation matrix consists of bounded component fields and hence its matrix L_2 norm is bounded. This implies that if the symmetrized adjoint is bounded, then the conservative adjoint is also bounded.

Energy Analysis. To study how the adjoint diverges, the time derivative of the adjoint energy $E\hat{v} = \|\hat{v}\|_{L_2(D)}$ is analyzed. The adjoint energy is basically the sum of the squares of the componentwise L_2 norms. The norms can be summed without dimensional scaling as the components of the symmetrized adjoint field have the same dimensions because of the fact that all the symmetrized Navier–Stokes variables have the same dimensions

$$-\frac{1}{2}\frac{dE_{\hat{v}}}{dt} = -\frac{1}{2}\frac{\partial}{\partial t}\left(\int_V \hat{v}_i\hat{v}_i\right)dV = -\int_V \hat{v}_i\frac{\partial \hat{v}_i}{\partial t}dV \tag{38}$$

premultiplying the adjoint equation by $\hat{v}_i$ and integrating over the entire domain

$$\frac{dE_{\hat{v}}}{dt} = \int_V \hat{v}_i\left(\hat{A}_{kji}\frac{\partial \hat{v}_k}{\partial x_j} + (B_{kjil} - B_{kjli})\frac{\partial v_l}{\partial x_j}\hat{v}_k + \frac{\partial}{\partial x_l}\left(\hat{D}_{kjil}\frac{\partial \hat{v}_k}{\partial x_j}\right)\right)dV \tag{39}$$

using $B_{kjil} = \partial \hat{A}_{kji}/\partial v_l$ the first term can be rewritten as

$$\int_V \hat{v}_i\hat{A}_{kji}\frac{\partial \hat{v}_k}{\partial x_j}dV = \int_S \hat{v}_i\hat{A}_{kji}\hat{v}_k n_j dS - \int_V \frac{\partial \hat{v}_i}{\partial x_j}\hat{A}_{kji}\hat{v}_k dV - \int_V \hat{v}_i B_{kjil}\frac{\partial v_l}{\partial x_j}\hat{v}_k dV \tag{40}$$

Using symmetry of $\hat{A}_{kji}$ in i and k

$$\int_V \hat{v}_i\hat{A}_{kji}\frac{\partial \hat{v}_k}{\partial x_j}dV = \frac{1}{2}\left(\int_S \hat{v}_i\hat{A}_{kji}\hat{v}_k n_j dS - \int_V \hat{v}_i B_{kjil}\frac{\partial v_l}{\partial x_j}\hat{v}_k dV\right) \tag{41}$$

The second term in the energy equations is

$$\int_V \frac{\partial}{\partial x_l}\left(\hat{D}_{kjil}\frac{\partial \hat{v}_k}{\partial x_j}\right)dV = \int_S \hat{v}_i\hat{D}_{kjil}\frac{\partial \hat{v}_k}{\partial x_j}n_l dS - \int_V \frac{\partial \hat{v}_i}{\partial x_l}\hat{D}_{kjil}\frac{\partial \hat{v}_k}{\partial x_j}dV \tag{42}$$

So, the adjoint energy equation becomes

$$\begin{aligned}\frac{dE\hat{v}}{dt} = &\int_V \hat{v}_i\left[\left(\frac{B_{kjil}}{2} - B_{kjli}\right)\frac{\partial v_l}{\partial x_j}\right]\hat{v}_k dV \\ &- \int_V \frac{\partial \hat{v}_i}{\partial x_l}\hat{D}_{kjil}\frac{\partial \hat{v}_k}{\partial x_j}dV + \int_S \hat{v}_i\left(\hat{D}_{kjil}\right)\frac{\partial \hat{v}_k}{\partial x_j}n_l dS \\ &+ \frac{1}{2}\int_S \hat{v}_i\hat{A}_{kji}\hat{v}_k n_j dS\end{aligned} \tag{43}$$

Let

$$\begin{aligned}\boldsymbol{M}_1 &= \frac{B_{kjil}}{2}\frac{\partial v_l}{\partial x_j} = \frac{\partial \hat{A}_{kji}}{\partial q_l}\frac{\partial q_l}{\partial x_j} \\ \boldsymbol{M}_2 &= B_{kjli}\frac{\partial v_l}{\partial x_j} = \frac{\partial \hat{A}_{kjl}}{\partial q_m}\frac{\partial q_m}{\partial v_i}\frac{\partial v_l}{\partial x_j} = \frac{\partial \hat{A}_{kjl}}{\partial q_m}S^{-1}_{mi}\frac{\partial v_l}{\partial x_j}\end{aligned} \tag{44}$$

The first volumetric term in 43 is a quadratic term in $\hat{\mathbf{v}}$, scaled by the matrix $\boldsymbol{M} = \boldsymbol{M}_1 - \boldsymbol{M}_2$. This is the term that primarily contributes to the diverging growth of the adjoint energy.

The second volumetric term in Eq. (43) is the dissipation term. Simplification shows that it is proportional to $\|\nabla \hat{v}_i\|^2$ scaled by the viscous coefficient. As the sign in front of the term is negative, this term reduces the growth of the adjoint energy.

The boundary terms are quadratic and can potentially contribute to the growth of the adjoint energy. On the inlet and outlet of the domain, Euler's equation-based characteristic boundary conditions are applied, as the fluid is practically inviscid on these boundaries. Using these boundary conditions, the first boundary term in Eq. (43) can be ignored. Denoting the characteristic Navier–Stokes variables by z_i, and the characteristic adjoint variables by $\hat{z}_i$, the boundary condition on the inlet and outlet can be written as

$$\hat{v}_k\hat{A}_{kji}n_j\delta v_i = \hat{z}_k\Lambda_{li}\delta z_i = 0 \tag{45}$$

using the eigendecomposition of $\hat{A}_{kji}n_j = Q_{kl}\Lambda_{lm}Q_{im}$ and the identities $\delta v_i = Q_{ki}\delta z_i, \hat{z}_i = Q_{ki}\hat{v}_k$. On the inlet, the characteristic variables coming into the domain are set. This corresponds to $\delta z_i = 0$, for i, where ith characteristic (or eigenvalues in the eigendecomposition) is negative. This in turn implies that $\hat{z}_j = 0$, for j, where the jth characteristic is positive, ensuring that the product is 0. This means that $\hat{\mathbf{v}}$ belongs to the negative eigenspace of the matrix, and so, the second boundary term is always negative. Similarly, for the outlet, the outgoing characteristics are set, which corresponds to $\delta z_i = 0$, for i, where ith characteristic is negative. Hence, for characteristic boundaries, the second boundary term is always negative and it does not contribute to the growth of the adjoint. Wall boundaries require more analysis, as in this case the viscous terms are important due to the presence of large gradients near the wall. For this paper, the walls are assumed to not contribute significantly to the growth of the adjoint term. This does not mean that the near wall regions adjoint fields do not contribute to the sensitivity, in fact, as we shall see in the Results section, they do.

The contribution from the objective source terms to the adjoint energy is linear and hence they do not directly contribute to the divergence of the adjoint fields.

Setting

$$b = \frac{c}{\sqrt{\gamma}}, a = \sqrt{\frac{\gamma - 1}{\gamma}}c$$

$$\boldsymbol{M}_1 = \frac{1}{2}\begin{pmatrix} \nabla\cdot u & \nabla_1 b & \nabla_2 b & \nabla_3 b & 0 \\ \nabla_1 b & \nabla\cdot u & 0 & 0 & \nabla_1 a \\ \nabla_2 b & 0 & \nabla\cdot u & 0 & \nabla_2 a \\ \nabla_3 b & 0 & 0 & \nabla\cdot u & \nabla_3 a \\ 0 & \nabla_1 a & \nabla_2 a & \nabla_3 a & \nabla\cdot u \end{pmatrix} \tag{46}$$

$$\boldsymbol{M}_2 = \begin{pmatrix} 0 & \frac{b}{\rho}\nabla_1\rho & \frac{b}{\rho}\nabla_2\rho & \frac{b}{\rho}\nabla_3\rho & \frac{\sqrt{\gamma-1}}{2}\nabla\cdot u \\ 0 & \nabla_1 u_1 & \nabla_2 u_1 & \nabla_3 u_1 & \frac{a}{2p}\nabla_1 p \\ 0 & \nabla_1 u_2 & \nabla_2 u_2 & \nabla_3 u_2 & \frac{a}{2p}\nabla_2 p \\ 0 & \nabla_1 u_3 & \nabla_2 u_3 & \nabla_3 u_3 & \frac{a}{2p}\nabla_3 p \\ 0 & \frac{2}{\gamma-1}\nabla_1 a & \frac{2}{\gamma-1}\nabla_2 a & \frac{2}{\gamma-1}\nabla_3 a & \frac{\gamma-1}{2}\nabla\cdot u \end{pmatrix} \tag{47}$$

Analyzing the matrix $\boldsymbol{M}$, which is the growth matrix, provides a way to find regions in the fluid flow where the adjoint is diverging. Using Cauchy–Schwartz inequality for matrix/vector norms

$$|\hat{\mathbf{v}}^{\mathrm{T}}\mathbf{M}\hat{\mathbf{v}}| \leq \|\mathbf{v}\|\|\mathbf{M}\mathbf{v}\| \tag{48}$$

Using the matrix induced two-norm and the identity $\|\mathbf{M}\mathbf{v}\|_2 \leq \sigma_1\|\mathbf{v}\|_2$, with σ_1 being the maximum singular value of $\boldsymbol{M}$

Downloaded From: http://turbomachinery.asmedigitalcollection.asme.org/ on 04/12/2018 Terms of Use: http://www.asme.org/about-asme/terms-of-use

$$|\hat{\mathbf{v}}^{\mathrm{T}}\mathbf{M}\hat{\mathbf{v}}| \leq \sigma_1 \|\hat{\mathbf{v}}\|_2^2 \tag{49}$$

The magnitude of σ_1 gives an indication of the regions where the adjoint energy growth is high. It has the dimensions $1/T$ and has the physical meaning of a rate of growth term.

Additional viscosity is added to the adjoint equations, curbing the divergence of the adjoint field, in the following form:

$$-\frac{\partial \hat{w}_i}{\partial t} - \left(A_{kji} - A^v_{kji}\right)\frac{\partial \hat{w}_k}{\partial x_j} = \frac{\partial}{\partial x_l}\left(\left(D_{kjil} + \lambda\sigma_1\delta_{ki}\delta_{jl}\right)\frac{\partial \hat{w}_k}{\partial x_j}\right) \tag{50}$$

where λ is a scaling factor that is problem specific, and in this work, is manually tuned. It has the dimensions of L^2, where L denotes length. As an initial estimate, the λ can be set to the length scale of the chaotic flow that contributes to the divergence of the adjoint. For example, for the turbine case, it is equal to the turbulent length scale in the wake. For 2D chaotic flow over a cylinder, it can be the length scale of the vortex shedding.

As the adjoint implementation is a discrete adjoint, which is obtained using automatic differentiation, there is no explicit function or equation which can be modified to add the artificial viscosity. So, viscosity is added by performing an extra implicit time integration step with a weighted Laplacian operator, after the explicit Runge–Kutta (RK) adjoint iteration. The boundary conditions for the implicit step are Dirichlet, using the values obtained from the explicit step. The overall time integration method can be described as an implicit–explicit (IMEX) Euler–RK scheme.

Results. The stabilized adjoint algorithm is tested on the 2D turbine vane problem. The objective is the time-averaged and mass flow-averaged pressure loss coefficient given by Eq. (1). Time-averaging is performed over 1/10th of a fluid flow through time.

Figure 8 shows the regions where the maximum singular value σ_1 of the matrix M is large. As expected, the region in the boundary layer near the trailing edge is primarily responsible for the diverging adjoint, and by adding additional dissipation in this region, we can restrict the growth of the adjoint field.

Various values of λ are tried from $\lambda = 10^{-4}$ to 10^{-2}. Figure 9 demonstrates the growth of energy norm of adjoint fields backward in time, for different values of λ. When the scaling factor is too low, the additional viscosity does not change the adjoint solution by a significant amount, and the L_2 norm of the adjoint fields stays high. On increasing the scaling factor, the magnitude of the L_2 norm of the adjoint fields reduces, but still shows exponential growth. This brings the order of the adjoint sensitivity to match the order of the finite difference sensitivity. Further increase in the scaling factor halts the exponential growth of the energy norm of the adjoint fields, reaching an approximately steady level. The adjoint sensitivity in this regime agrees with the finite difference sensitivity by an error of less than 20%.

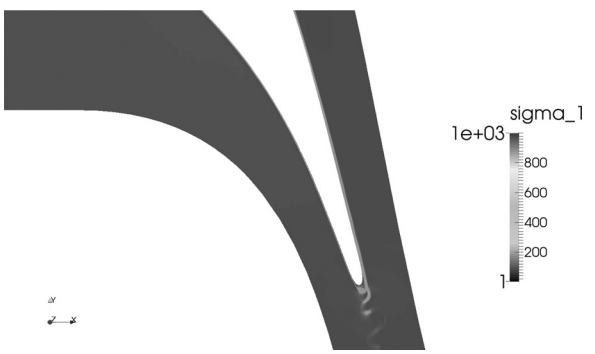

Fig. 8 Contour plot of divergence indicator σ_1 for the turbine vane, normalized by inverse of a single flow through time

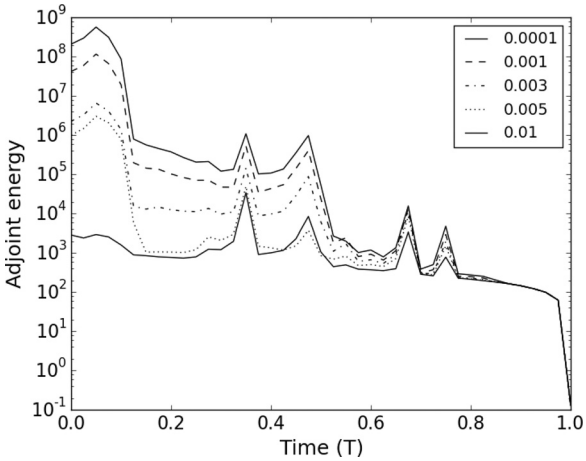

Fig. 9 Growth of energy norm of adjoint for various scaling factors. *X*-axis is time normalized by a single flow through time.

Table 2 Comparison of adjoint and finite difference sensitivity for various scaling factors

Sensitivities		
Scaling factor (λ)	Finite difference	Adjoint
0.0001	1.71×10^{-4}	3.44×10^{-3}
0.0004	1.71×10^{-4}	5.42×10^{-4}
0.0006	1.71×10^{-4}	-1.7×10^{-4}
0.001	1.71×10^{-4}	-4.5×10^{-4}
0.003	1.71×10^{-4}	1.30×10^{-4}
0.005	1.71×10^{-4}	1.71×10^{-4}
0.007	1.71×10^{-4}	1.59×10^{-4}
0.01	1.71×10^{-4}	1.42×10^{-4}

Table 2 and Fig. 10 show the relative error in adjoint sensitivity with respect to the finite difference sensitivity, for a Gaussian-shaped source term perturbation, upstream of the leading edge of the vane, to the conservative compressible Navier–Stokes equations. The length scale of the perturbation is 10 mm, and its relative magnitude to the convective term of the Navier–Stokes equation is around 1%. From Table 2, it can be seen that there seems to be an optimal value of $\lambda = 0.005$, and raising it beyond this point leads to a slowly increasing error in the sensitivities. This is due to the fact that too much viscosity is being added to the adjoint equations, making the adjoint sensitivities inaccurate. There is a sizable range of scaling factors where the adjoint flow

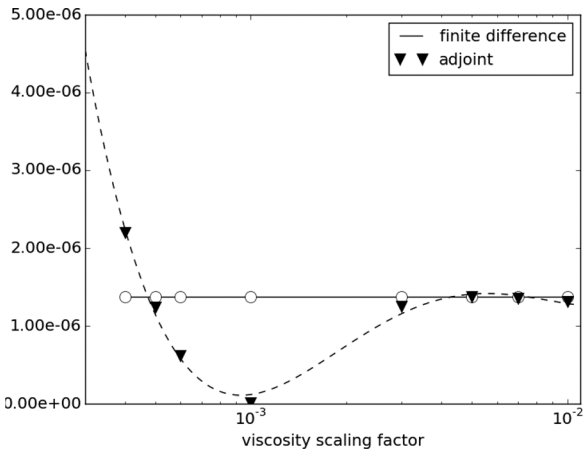

Fig. 10 Error in adjoint sensitivity for various scaling factors

Downloaded From: http://turbomachinery.asmedigitalcollection.asme.org/ on 04/12/2018 Terms of Use: http://www.asme.org/about-asme/terms-of-use

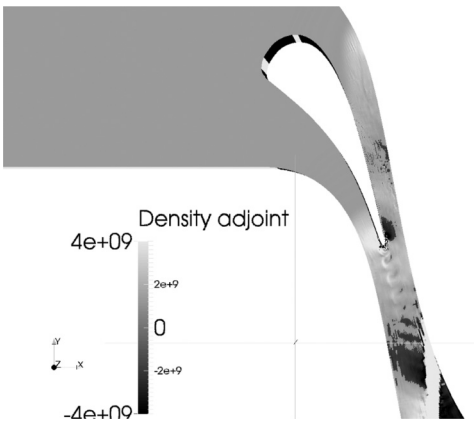

Fig. 11 Density adjoint solution at $t = 0$

field is sufficiently damped and the sensitivities are reasonably correct.

Figure 11 shows a visualization of the density adjoint field at $t = 0$ (terminal time for the adjoint simulation). The magnitude of the adjoint field is large in the trailing edge regions, in the beginning of the wake and near the region where the averaging of the design objective is performed.

As the results show, selection of the scaling factor λ greatly influences the adjoint sensitivities obtained. After using an initial estimate for λ, obtained from the process described in the previous section, Energy Analysis, multiple values of λ need to be tried to get a set of stabilized adjoint flow simulations. Using this set, Richardson extrapolation, a technique used in many numerical algorithms [23,24], can be used to improve the accuracy of adjoint sensitivities and obtain an error estimate.

Let $g(\lambda)$ be the computed sensitivity, g^* be the true sensitivity, representing g using a polynomial expression

$$g(\lambda) = g^* + a\lambda + b\lambda^2 + \cdots + O(\lambda^n) \tag{51}$$

Let $g_{i+1}(\lambda) = h^i g_i(\lambda/h) - g_i(\lambda)/h^i - 1$ with $g_0 = g$. Then

$$g_{i+1}(\lambda) = g^* + O(\lambda^{i+1}) \tag{52}$$

So, by utilizing multiple adjoint sensitivities from simulations with different scaling factors, a more accurate gradient can be estimated. Though running multiple adjoint simulations is expensive, it is still much cheaper than all of the other sensitivity analysis methods for chaotic systems. This technique has the potential to make the viscous-stabilized adjoint method more useful for generic chaotic or turbulent fluid flow problems.

Conclusion

The unsteady adjoint method is useful for computing sensitivities of objectives to a large number of parameters. The unsteady adjoint solution diverges to infinity due to chaotic dynamics of turbulence in fluid flows. An energy analysis provides valuable information about the mechanism of growth of the adjoint field. Local artificial viscosity can limit the divergence adjoint field and maintain accuracy of adjoint sensitivities. The viscous stabilized unsteady adjoint method provides a promising method for computing adjoint sensitivities of long time-averaged objectives, with respect to arbitrary perturbations, for a turbulent fluid flow. The effectiveness of the method has been demonstrated on 2D chaotic flow problems and will be extended to 3D flow problems. The estimation of the optimal scaling factor for a particular fluid problem requires more work, and will be investigated in the future with the help of Richardson extrapolation.

Acknowledgment

This research used resources of the Oak Ridge Leadership Computing Facility at Oak Ridge National Laboratory, which is supported by the Office of Science of the Department of Energy under Contract No. DE-AC05-00OR22725.

Nomenclature

a, b = scaled speeds of sound
$\mathbf{A}$ = Jacobian of convective flux three-dimensional tensor
$\hat{\mathbf{A}}$ = primitive flux three-dimensional tensor for symmetrized variables
$\mathbf{A}^{\mathbf{v}}$ = Jacobian of viscous flux three-dimensional tensor
$\mathbf{B}$ = Jacobian of $\hat{\mathbf{A}}$ with respect to symmetrized variables
c = speed of sound
D = domain for the fluid problem
$\mathbf{D}$ = Jacobian of viscous flux with respect to gradient terms four-dimensional tensor
$\hat{\mathbf{D}}$ = viscous four-dimensional tensor
e = internal energy
E = total energy
$E\hat{v}$ = L_2 norm of adjoint of symmetrized variables
$\mathbf{F}$ = Navier–Stokes convective flux vector
$\mathbf{F}^{\mathbf{v}}$ = Navier–Stokes viscous flux vector
J = instantaneous objective
$\bar{J}$ = time-averaged objective
L = length scale of fluid problem
M, M_1, M_2 = growth matrix of adjoint energy
M_p = Mach number on downstream plane
p_p = pressure on downstream plane
$p_{t,p}$ = stagnation pressure on downstream plane
$\bar{p}_l$ = pressure loss objective
$\bar{p}_{t,l}$ = mass-averaged stagnation pressure loss on downstream plane
$\bar{p}_{t,\text{in}}$ = stagnation pressure at the inlet
$\mathbf{q}$ = primitive variables vector
$\mathbf{s}$ = Navier–Stokes equations source term vector
S = surface area of boundary
$\mathbf{S}$ = transformation matrix from primitive to symmetrized variables
T = time-averaging interval
$\mathbf{T}$ = transformation matrix from conservative to symmetrized variables
$\mathbf{u}$ = velocity vector
$\mathbf{v}$ = symmetrized variables vector
V = volume of domain
$\mathbf{V}$ = transformation matrix from conservative to primitive variables
$\hat{\mathbf{v}}$ = adjoint for symmetrized variables
$\mathbf{w}$ = conservative variables vector
$\hat{\mathbf{w}}$ = adjoint of conservative variables
$\mathbf{x}$ = position vector
α = thermal coefficient
γ = isentropic expansion factor
λ = scaling factor for additional adjoint viscosity
μ = viscosity coefficient
ρ = density at a point in the domain
ρ_p = density on downstream plane
$\boldsymbol{\sigma}$ = viscous stress tensor
σ_1 = maximum singular value of growth matrix

References

[1] Gourdain, N., Gicquel, L. Y., and Collado, E., 2012, "Comparison of RANS and LES for Prediction of Wall Heat Transfer in a Highly Loaded Turbine Guide Vane," J. Propul. Power, **28**(2), pp. 423–433.
[2] Jameson, A., 1995, "Optimum Aerodynamic Design Using CFD and Control Theory," AIAA Paper No. 95-1729.
[3] Lyu, Z., and Martins, J. R., 2014, "Aerodynamic Design Optimization Studies of a Blended-Wing-Body Aircraft," J. Aircr., **51**(5), pp. 1604–1617.

Downloaded From: http://turbomachinery.asmedigitalcollection.asme.org/ on 04/12/2018 Terms of Use: http://www.asme.org/about-asme/terms-of-use

[4] Economon, T. D., Palacios, F., and Alonso, J. J., 2013, "A Viscous Continuous Adjoint Approach for the Design of Rotating Engineering Applications," AIAA Paper No. 2013-2580.
[5] Wang, Q., and Gao, J.-H., 2013, "The Drag-Adjoint Field of a Circular Cylinder Wake at Reynolds Numbers 20, 100 and 500," J. Fluid Mech., **730**, pp. 145–161.
[6] Blonigan, P., Chen, R., Wang, Q., and Larsson, J., 2012, "Towards Adjoint Sensitivity Analysis of Statistics in Turbulent Flow Simulation," Stanford Center of Turbulence Research Summer Program, p. 229.
[7] Aceves, A., Adachihara, H., Jones, C., Lerman, J. C., McLaughlin, D. W., Moloney, J. V., and Newell, A. C., 1986, "Chaos and Coherent Structures in Partial Differential Equations," Phys. D: Nonlinear Phenom., **18**(1), pp. 85–112.
[8] Wilcox, D. C., 1998, *Turbulence Modeling for CFD*, Vol. 2, DCW Industries, La Canada, CA.
[9] Arts, T., and de Rouvroit, M. L., 1992, "Aero-Thermal Performance of a Two-Dimensional Highly Loaded Transonic Turbine Nozzle Guide Vane: A Test Case for Inviscid and Viscous Flow Computations," ASME J. Turbomach., **114**(1), pp. 147–154.
[10] Lea, D. J., Allen, M. R., and Haine, T. W., 2000, "Sensitivity Analysis of the Climate of a Chaotic System," Tellus A, **52**(5), pp. 523–532.
[11] Thuburn, J., 2005, "Climate Sensitivities Via a Fokker–Planck Adjoint Approach," Q. J. R. Meteorol. Soc., **131**(605), pp. 73–92.
[12] Ruelle, D., 2008, "Differentiation of SRB States for Hyperbolic Flows," Ergodic Theory Dyn. Syst., **28**(02), pp. 613–631.
[13] Ruelle, D., 2009, "A Review of Linear Response Theory for General Differentiable Dynamical Systems," Nonlinearity, **22**(4), p. 855.
[14] Blonigan, P., Gomez, S., and Wang, Q., 2014, "Least Squares Shadowing for Sensitivity Analysis of Turbulent Fluid Flows," preprint arXiv:1401.4163.
[15] Garnier, E., Adams, N., and Sagaut, P., 2009, *Large Eddy Simulation for Compressible Flows*, Springer Science & Business Media, Medford, MA.
[16] Moeng, C.-H., and Wyngaard, J. C., 1989, "Evaluation of Turbulent Transport and Dissipation Closures in Second-Order Modeling," J. Atmos. Sci., **46**(14), pp. 2311–2330.
[17] Macdonald, C. B., 2003, "Constructing High-Order Runge-Kutta Methods With Embedded Strong-Stability-Preserving Pairs," Ph.D. thesis, Simon Fraser University, Burnaby, BC.
[18] Roe, P. L., 1981, "Approximate Riemann Solvers, Parameter Vectors, and Difference Schemes," J. Comput. Phys., **43**(2), pp. 357–372.
[19] Choi, H., and Moin, P., 2012, "Grid-Point Requirements for Large Eddy Simulation: Chapman's Estimates Revisited," Phys. Fluids (1994-Present), **24**(1), p. 011702.
[20] Bastien, F., Lamblin, P., Pascanu, R., Bergstra, J., Goodfellow, I. J., Bergeron, A., Bouchard, N., and Bengio, Y., 2012, "Theano: New Features and Speed Improvements," Deep Learning and Unsupervised Feature Learning NIPS 2012 Workshop, p. 5590.
[21] Bergstra, J., Breuleux, O., Bastien, F., Lamblin, P., Pascanu, R., Desjardins, G., Turian, J., Warde-Farley, D., and Bengio, Y., 2010, "Theano: A CPU and GPU Math Expression Compiler," Python for Scientific Computing Conference (SciPy).
[22] Abarbanel, S., and Gottlieb, D., 1981, "Optimal Time Splitting for Two-and Three-Dimensional Navier-Stokes Equations With Mixed Derivatives," J. Comput. Phys., **41**(1), pp. 1–33.
[23] Ford, W. F., and Sidi, A., 1987, "An Algorithm for a Generalization of the Richardson Extrapolation Process," SIAM J. Numer. Anal., **24**(5), pp. 1212–1232.
[24] Celik, I., and Zhang, W.-M., 1995, "Calculation of Numerical Uncertainty Using Richardson Extrapolation: Application to Some Simple Turbulent Flow Calculations," ASME J. Fluids Eng., **117**(3), pp. 439–445.

Downloaded From: http://turbomachinery.asmedigitalcollection.asme.org/ on 04/12/2018 Terms of Use: http://www.asme.org/about-asme/terms-of-use